High Energy Density Physics 9 (2013) 419–424

Contents lists available at SciVerse ScienceDirect

High Energy Density Physics

journal homepage: www.elsevier.com/locate/hedp

A hybrid detailed level and configuration accounting model for investigating the radiative opacity of gold plasmas with open 4*d* and 4*f* shells

Cheng Gao [a], Jiaolong Zeng [a,*], Fengtao Jin [a], Jianmin Yuan [a,b]

[a] Department of Physics, College of Science, National University of Defense Technology, Changsha 410073, Hunan, PR China
[b] State Key Laboratory of High Performance Computing, National University of Defense Technology, Changsha 410073, Hunan, PR China

ARTICLE INFO

Article history:
Received 9 March 2013
Accepted 9 March 2013
Available online 10 April 2013

Keywords:
Radiative opacity
Gold plasma
Hybrid model

ABSTRACT

A hybrid model combining the detailed level accounting (DLA) and detailed relativistic configuration accounting (DCA) methods is developed to investigate the radiative opacity of gold plasmas with open 4*d* and 4*f* shells. Due to the collapse of 4*f* shells, the configurations with multi-electron excited from 4*d* and 4*f* shells are bound and can form a huge number of fine-structure levels and detailed transition lines. A full DLA calculation is time-consuming and intractable and thus a hybrid DLA and DCA method is needed. To obtain accurate radiative opacity, the transitions within the collapsed orbitals and transitions to the relatively lowly excited orbitals are treated by a DLA method, while the transitions to the higher excited orbitals are treated by a DCA method. As an illustrative example, the spectrally resolved, Rosseland and Planck mean opacity of gold plasmas at 100 eV and 0.001 g/cm^3 are calculated by using the hybrid model. The present results are compared with those obtained by pure DCA and average atom models, where large discrepancies in the line intensities and positions are found for the strongest 4*d*–4*f* transitions due to the collapse of 4*f* shells indicating the importance of detailed treatment to obtain the accurate opacity.

1. Introduction

Radiative opacity of gold plasmas is of great significance in research fields such as inertial confinement fusion (ICF) [1–3]. In indirectly driven ICF experiments, the inside wall of hohlraum is usually made of gold material. It is irradiated by high power lasers and the gold plasma produced emits strong X-ray radiation to drive the capsule implosion. In order to understand the physics processes, such as energy transfer in the gold hohlraum cavity, and to optimize the design of the hohlraum and target, knowledge of the radiative opacity of gold plasmas is very important in ICF experiments. Dewald et al. [4] carried out the first gold hohlraum experiment on the National Ignition Facility (NIF) to test radiation temperature limits imposed by plasma filling and showed that radiative opacity plays a key role in the hydrodynamic simulations used to analyze the experimental results.

It is a great challenge, however, to investigate the radiative opacity of gold plasmas, both experimentally and theoretically. Experimentally, on one hand, it is difficult to obtain a local thermodynamic equilibrium (LTE) plasma, and on the other hand, the greatly increased re-emission of such high-Z plasmas makes accurate measurement difficult. To our knowledge, there are only a few experimental results on gold opacity reported in literature [5,6]. Eidmann et al. [5] measured the opacity of a gold plasma at a density of ~0.01 g/cm^3 and a relatively low temperature of ~20 eV. Recently, Zhang et al. [6] reported measurements of the opacity of a gold plasma at a density of 0.02 g/cm^3 and a higher temperature of 85 eV. Theoretically, it is very difficult to calculate the radiative opacity of gold plasmas due to the complicated electronic structure of gold ions. Most theoretical research was carried out by using various statistical models employing unresolved transition arrays (UTA) [7], super-transition arrays (STA) [8] and the average atom (AA) [9,10]. However, there are systematic discrepancies between experimental and theoretical results obtained by statistical models [5,6]. In order to explain the discrepancies, a more accurate method such as detailed-level-accounting (DLA) model is needed. By using a DLA model, we successfully reproduced the transmission spectra of gold plasma measured by Eidmann et al. [5] and pointed out the physical origin of discrepancies between experiment and theory for the first time [11,12]. The DLA method was also applied to study the radiative opacity of gold plasmas at high temperatures (≥1000 eV)

* Corresponding author.
E-mail addresses: gaocheng@nudt.edu.cn (C. Gao), jiaolongzeng@hotmail.com (J. Zeng), jmyuan@nudt.edu.cn (J. Yuan).

1574-1818/$ – see front matter © 2013 Elsevier B.V. All rights reserved.
http://dx.doi.org/10.1016/j.hedp.2013.03.010

[13]. The detailed calculation for such high-Z plasmas is very time-consuming and hybrid models were developed in the past decades to balance the accuracy and computational time [14–16]. Yan et al. [14] calculated the opacity of high-Z material and gold mixtures at high temperatures by using a mixed detailed configuration accounting (DCA) and UTA model. Porcherot et al. [15] used a mixed DLA and STA method to calculate the opacities of mid-Z plasmas. For non-LTE gold plasmas, large discrepancies were also found for charge state distribution (CSD) and emission properties between theoretical and experimental results (see the NLTE workshops [17–21]). Our recent work, based on a detailed relativistic configuration approach, shows good agreement with the experiments [22].

In our full DLA calculations for the radiative opacity, the ions in gold plasmas are either weakly ionized or very highly ionized, which have either closed 4*d* and 4*f* shells [11,12] or no 4*d* and 4*f* shells [13] in their ground configurations. With the development of large laser facilities, it is possible to create gold plasmas at temperatures from ~100 eV [6] to ~300 eV [23]. For such a temperature range, the ions in gold plasmas tend to have open 4*d* or 4*f* shells. It is a challenge for theorists to calculate the radiative opacity of gold plasmas when ion stages with open 4*d* or 4*f* shells are involved. This is because the 4*f* orbital of these gold ions normally collapses and therefore the multi-electron excited configurations from 4*d* and 4*f* orbitals are still bound. These bound configurations can split into a huge number of fine-structure levels and consequently a huge number of radiative transitions between these levels are generated, which may make a full DLA investigation intractable. Therefore, it is necessary to develop a hybrid DLA and DCA model to calculate the radiative opacity of gold plasmas. For the transitions within collapsed orbitals and to relatively low excitation orbitals, the electronic correlation effects are important. Therefore, a DCA description is not adequate and we adopt a DLA formalism. For the transitions to highly excited orbitals, a DCA description is usually sufficiently accurate. In this work, we will demonstrate such a hybrid method to calculate the radiative opacity of gold plasmas with open 4*d* or 4*f* shells. As an illustrative example, the radiative opacities of a gold plasma at 100 eV and 0.001 g/cm^3 are obtained by using our recently developed hybrid model and compared with the results obtained by AA and a pure DCA methods. The large discrepancies in the strongest 4*d*–4*f* transitions between the present hybrid and statistical models (AA and DCA) indicate the importance of the detailed treatment for the transitions within the collapsed orbitals.

2. Theoretical method

The detailed theories of radiative opacity can be seen elsewhere [12,24] and here we only give an outline. For an LTE plasma at temperature T and mass density ρ, the total radiative opacity at photon energy $h\nu$ is given by

$$\rho\kappa'(h\nu) = \left(\mu_{\rm bb}(h\nu)+\mu_{\rm bf}(h\nu)+\mu_{\rm ff}(h\nu)\right)\left(1-e^{-h\nu/kT}\right) + \mu_{\rm scatt}(h\nu), \quad (1)$$

where $\mu_{\rm bb}$, $\mu_{\rm bf}$, $\mu_{\rm ff}$ and $\mu_{\rm scatt}$ are absorption coefficients from bound–bound, bound–free, free–free and scattering processes, respectively. The prime on the opacity means that stimulated emission has been taken into account.

The bound–bound absorption coefficient can be written by

$$\mu_{\rm bb}(h\nu) = \sum_i \sum_{ll'} N_{il}\sigma_{ill'}(h\nu), \quad (2)$$

where N_{il} is the population density of level l of ionization stage i and $\sigma_{ill'}(h\nu)$ is the cross section of photoexcitation from level l to l' of ionization stage i. In the calculation by DCA method, l and l' represent the relativistic configurations. $\sigma_{ill'}(h\nu)$ can be expressed in terms of the absorption oscillator strength $f_{ill'}$ as

$$\sigma_{ill'}(h\nu) = \frac{\pi h e^2}{m_{\rm e}c} f_{ill'} S(h\nu), \quad (3)$$

where $f_{ill'}$ is the absorption oscillator strength, h is the Planck constant, c is the speed of light in vacuum, e is the electron charge, $m_{\rm e}$ is the mass of an electron, and $S(h\nu)$ is the line shape function which is taken to be the Voigt profile with electron impact broadening and Doppler broadening included. Under the assumption of LTE, the CSD is determined by Saha–Boltzmann equation [25]

$$\frac{N_{i+1}N_{\rm e}}{N_i} = \frac{Z_{\rm e}Z_{i+1}}{Z_i} e^{-(\phi_i-\Delta\phi_i)/kT}, \quad (4)$$

where N_i and $N_{\rm e}$ are the density of ionization stage i and free electrons, Z_i and $Z_{\rm e}$ are the partition function of ionization stage i and free electrons, respectively, and ϕ_i and $\Delta\phi_i$ are the ionization potential (IP) and ionization potential depression (IPD) of ionization stage i, respectively. The IPD is obtained by Stewart–Pyatt (S–P) model [26]. In this work, the atomic data such as energy levels and oscillator strengths in the fine-structure level and relativistic configuration approaches are obtained by using Flexible Atomic Code (FAC) [27] where a fully relativistic approach based on the Dirac equation is used throughout the entire package and the code provides two modes of calculation based on detailed levels and relativistic configurations.

In many practical applications, the mean opacities such as Rosseland ($K_{\rm R}$) and Planck ($K_{\rm P}$) mean opacities are needed, which are defined by

$$\frac{1}{K_{\rm R}} = \int_0^\infty \frac{W_{\rm R}(u){\rm d}u}{\kappa'(u)}, \quad (5)$$

and

$$K_{\rm P} = \int_0^\infty (\kappa'(u)-\kappa_{\rm scatt}(u))W_{\rm P}(u){\rm d}u, \quad (6)$$

where $u = h\nu/kT$, $W_{\rm R}$ and $W_{\rm P}$ are Rosseland and Planck weighting functions, respectively.

3. Results and discussions

A complete DLA calculation of radiative opacity is complex for gold plasmas with open 4*f* or 4*d* shells due to the collapse of 4*f* orbitals. The ion stages with open 4*f* or 4*d* shells range from Au^{20+} (ground configuration ([Ni])$4s^24p^64d^{10}4f^{13}$) to Au^{42+} (ground configuration ([Ni])$4s^24p^64$d), where [Ni] means $1s^22s^22p^63s^23p^63d^{10}$. For these gold ions, the 4*f* orbital is collapsed. Fig. 1 shows the wave functions of 4*s*, 4*p*, 4*d*, and 4*f* orbitals for a few representative gold ions of (a) Au^{20+} (with ground configuration $4s^24p^64d^{10}4f^{13}$), (b) Au^{26+} ($4s^24p^64d^{10}4f^7$), (c) Au^{32+} ($4s^24p^64$d$^{10}4f$), (d) Au^{34+} ($4s^24p^64d^9$), (e) Au^{38+} ($4s^24p^64d^5$) and (f) Au^{42+} ($4s^24p^64d$). It can be seen that the 4*f* orbital is pulled strongly inward toward the nucleus, which is an indication of orbital collapse. Such an inward shift becomes stronger and stronger with the increase of ion stages. Although only representative examples are given in Fig. 1, the effects of orbital collapse are a common phenomenon for all gold ions from Au^{20+} to Au^{42+}. Due to the orbital collapse, the electronic correlation of the collapsed orbitals is

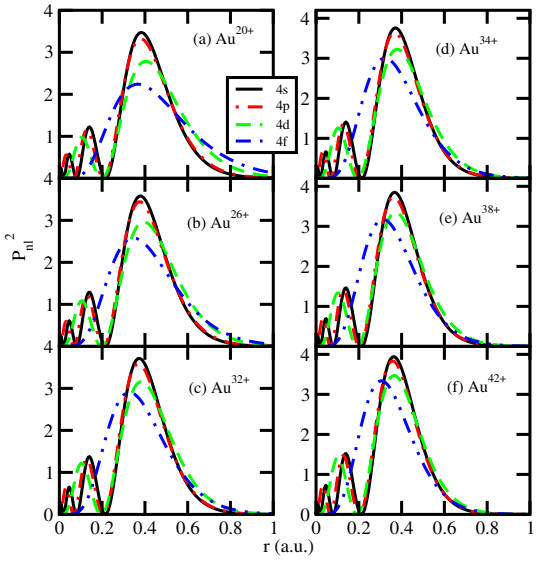

Fig. 1. The radial wave functions of 4*s*, 4*p*, 4*d*, and 4*f* orbitals of the ground configurations of (a) Au^{20+} ($4s^24p^64d^{10}4f^{13}$), (b) Au^{26+} ($4s^24p^64d^{10}4f^7$), (c) Au^{32+} ($4s^24p^64d^{10}4f$), (d) Au^{34+} ($4s^24p^64d^9$), (e) Au^{38+} ($4s^24p^64d^5$) and (f) Au^{42+} ($4s^24p^64d$).

usually strong and the detailed treatment taking this effect into account is necessary to obtain the accurate atomic data [28–30].

A direct consequence of the orbital collapse is that multi-electron excited states from 4*d* to 4*f* and/or from 4*p* to 4*d* are still bound states, and thus one must include their contributions to the opacity from numerous multiply excited states. As an illustrative example, Fig. 2 shows the level energies of a few configurations of Au^{28+} (ground configuration $4s^24p^64d^{10}4f^5$). The number beside each configuration denotes the number of levels and the dashed line represents the IP (967 eV) of Au^{28+}. To simplify the figure description, only the range of the level energy for non-relativistic configurations is shown as a rectangle box. For example, the level energy ranges from 0 eV to 56 eV with a total number of 198 levels for the ground configuration of $4s^24p^64d^{10}4f^5$ of Au^{28+}, with the energy of the ground level being taken to be reference value of 0 eV. Due to the collapse of 4*f* orbital, three 4*d* electrons being excited to 4*f* orbital and two or three 4*f* electrons to 5*s*, 5*p*, and 5*d* orbitals remain bound to the nucleus (which means their energies are lower than the IP). Thus, the number of bound configurations which contribute to the radiative opacity is large. As a descriptive example, Fig. 2 shows one such Rydberg series of $4s^24p^64d^84f^6nl$ (nl = 4*f*, 5*s*, 5*p*, 5*d* and 5*f*). For this series, the energies of all these two 4*d* electron excited configurations are lower than the IP except that a small part of levels belonging to $4s^24p^64d^84f^65f$ are above the IP. The level structures of this Rydberg series which is connected with the calculation of opacity are very complicated and therefore extraordinarily time-consuming. We take one configuration of $4s^24p^64d^84f^65d$ as an example to show the complexity of the problem. From this configuration, there are many transition arrays such as 4*f*–*ng*, 4*f*–*nd*, 4*d*–*nf*, 4*d*–*np*, 4*p*–*nd*, 4*p*–*ns*, and 4*s*–*np*. All these transition arrays only take contributions from absorption of 4*l* (l = *s*, *p*, *d* and *f*) electrons into account. To obtain a complete spectrally resolved opacity, one must also include those contributions from 3*d*, 3*p*, 3*s*, 2*p*, 2*s* and 1*s* electrons. Consider one transition array of $4s^24p^64d^84f^65d$–$4s^24p^64d^84f^65dng$ (n = 5–14), for which the number of levels for the initial configuration is 111,874, while that of each final configuration is about 100 times more. Only parallelized atomic structure codes can calculate the required atomic data for opacity in order to take into account the intra-configuration interaction into account. Making a simple estimate, the number of spectral lines for each of these transition array exceeds ten billions (1.0×10^{10}). As a result, that DLA treatment for these types of transition array is intractable and we need to resort to a DCA formalism.

To better understand our DLA and DCA hybrid formalism, we use the Au^{30+} (ground configuration $4s^24p^64d^{10}4f^3$) as an example. The present DCA calculations are based on the relativistic configurations. For this particular ion, the 4*d* orbital has the maximal number of electrons, and hence it provides a dominant contribution to the opacity. Among the transition arrays from 4*d* orbital, the strongest ones originate from 4*d*–*nf* (n = 4–15) transitions. In this work, the maximal principal quantum number n is taken to be 15 to ensure the results convergent. Fig. 3 shows the radiative opacity

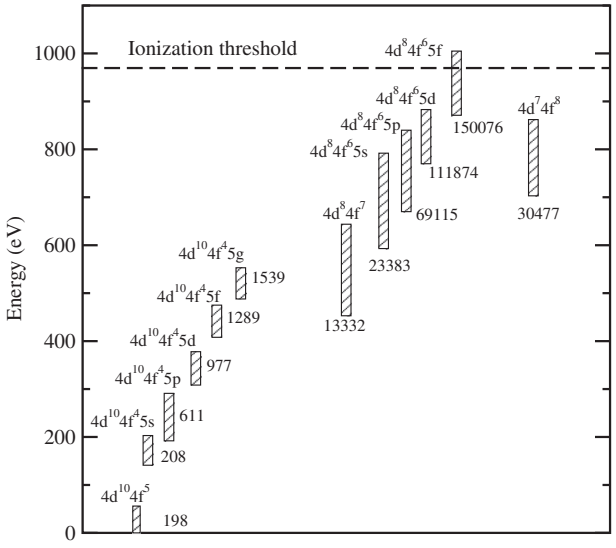

Fig. 2. The energy scheme of some configurations of Au^{28+}. The rectangle boxes represent the energy ranges of the configurations. The number beside each configuration denotes their number of fine-structure levels and the dashed line represents the ionization potential (IP) of Au^{28+}.

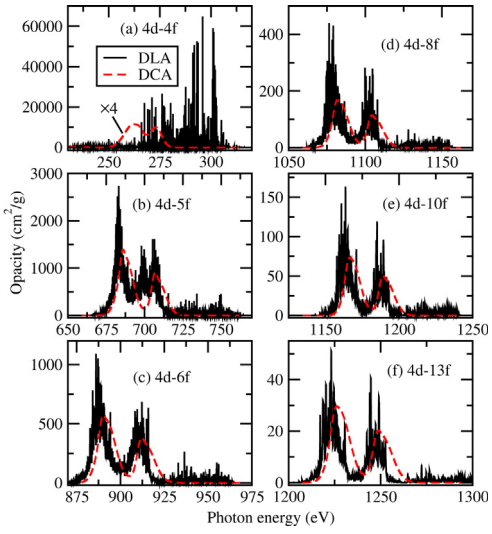

Fig. 3. The opacities of the 4*d*–*nf* transitions from the ground configuration of Au^{30+} at 100 eV and 0.001 g/cm^3 obtained by DLA (black) and DCA (red dashed) methods. The principle quantum number n = 4, 5, 6, 8, 10 and 13 in panels (a)–(f). In panel (a), the opacities obtained by DCA method are multiplied by a factor of 4 for more clearly viewing. (For interpretation of the references to color in this figure legend, the reader is referred to the web version of this article.)

contributed by $4d$–nf transition arrays, with $n = 4$, 5, 6, 8, 10, and 13, respectively, for panels (a)–(f), from the ground configuration $4s^24p^64d^{10}4f^3$ of Au^{30+} obtained by DLA and DCA methods for a plasma condition of mass density of 0.001 g/cm^3 and temperature of 100 eV. In panel (a), the opacity of $4d$–$4f$ transition array obtained by the DCA method is multiplied by a factor of 4 for a clearer viewing. From the inspection of Fig. 3, it can easily be seen that large discrepancies are found between the results of DLA and DCA methods for the $4d$–$4f$ transition array. Not only dose the DCA method under-estimate the opacity, it predicts that the line positions are at more than 20 eV lower photon energy. The reason for this discrepancy is that the DCA method neglects the intra-configuration interaction, while the DLA formalism includes the electronic correlation effects within mixed levels of single configuration. Such interactions are so strong that these must be taken into account for the calculation of basic atomic data such as level energy and oscillator strength. The collapse of $4f$ orbital is the main physical origin of these differences. The large discrepancies between DCA and DLA results for the $4d$–$4f$ transitions indicate that the DLA calculation is necessary for such $\Delta n = 0$ transition arrays. For the spectra of $4d$–nf ($n > 4$) transitions, it can be seen that there are two strong absorption structures which are caused by the spin-orbit splitting. In each panel from plot (b)–(f), the strongest structure in the lower photon energy range originates from transitions of $4d_{5/2}$–$4f_{7/2}$ and the relatively weaker structure in the higher photon energy range originates from $4d_{3/2}$–$4f_{5/2}$. The line positions of $4d$–nf ($n > 4$) predicted by DCA formalism are only about 3 eV lower than those predicted by the DLA methods. With the increase of the principle quantum number n, from panels (b) to (f), it can be seen that the contribution to the opacities is becoming smaller so that better agreement is found between the results predicted by the DCA and DLA method. Therefore, we can use the DCA formalism to calculate the opacity contributed by transition arrays of higher principle quantum number n.

In Fig. 3, the detailed level structures are evident. With the increase of mass density, the agreement between the DLA and DCA methods continuously improve and thus the DCA treatment becomes closer to the DLA (see Fig. 4). In Fig. 4, the population distribution is assumed the same as in Fig. 3, yet the temperature and density is taken to be 100 eV and 0.1 g/cm^3. It can be seen that the opacity obtained by the DCA method is nearly equal to that by DLA

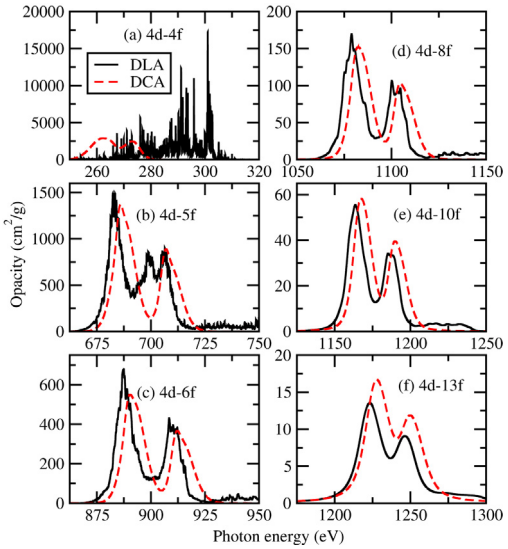

Fig. 4. Same to Fig. 3, but the electron impact broadenings are obtained at 100 eV and 0.1 g/cm^3.

formalism except for the ~3 eV energy shift toward higher photon energy for DCA results. We also investigated other transition arrays such as $4f$–ng/nd, $4p$–ns/nd, $4d$–np and $4s$–np by using DLA and DCA methods and similar conclusions can be drawn. Systematic comparisons between the results obtained by DLA and DCA methods indicate that our formalism for the hybrid DLA and DCA model is reasonable and adequate to investigate the radiative opacity of gold plasmas with open $4f$ and $4d$ shells.

In what follows, Au^{30+} is taken as an example to illustrate the detailed method of calculation in the hybrid DLA and DCA model. According to detailed calculations, we first determined the bound configurations of Au^{30+}, which are:

$4s^24p^64d^{10}4f^3$, $4s^24p^64d^{10}4f^2nl$ ($n \le 15$, $l \le n-1$), $4s^24p^64d^94f^4$, $4s^24p^64d^94f^3nl$ ($n \le 6$, $l \le n-1$), $4s^24p^54d^{10}4f^4$, $4s^24p^54d^{10}4f^3nl$ ($n \le 6$, $l \le n-1$), $4s4p^64d^{10}4f^4$, $4s^24p^64d^{10}4f5lnl'$ ($l \le 3$, $n \le 6$, $l' \le n-1$), $4s^24p^64d^84f^5$, $4s^24p^64d^84f^4nl$ ($n \le 6$, $l \le n-1$), $4s^24p^64d^74f^6$, $4s^24p^64d^94f^25lnl'$ ($l \le 3$, $n \le 6$, $l' \le n-1$), $4s^24p^64d^{10}5s^2nl$ ($n \le 6, l \le n-1$), $4s^24p^64d^{10}5s5pnl$ ($n \le 6, l \le n-1$) and $4s^24p^64d^{10}5p^2nl$ ($n \le 6$, $l \le n-1$).

As a second step, all possible transition arrays are constructed for the bound configurations given above according to the dipole selection rules, which leads to a large number of transition arrays. For transition arrays of $nl - n'l'$ with $\Delta n = n' - n \le 4$, we adopted a DLA method to calculate the required atomic data, while those with higher principal quantum numbers up to $n = 15$ are treated by a DCA method. The contributions of the transitions from highly excited Rydberg configurations ($4s^24p^64d^{10}4f^2nl$ ($10 \le n \le 15$, $l \le n-1$)) are relatively small compared with the lower excited configurations, so we chose the DCA method to calculate the relevant atomic data. The photoionization cross sections are obtained in the approximation of detailed relativistic configurations.

It should be noted that the configuration interaction (CI) is important to obtain accurate atomic data for such gold ions [31,32]. However, a large-scale CI calculation for such complicated ion stages with open $4d$ and $4f$ shells is time-consuming, to the point of intractability within the context of current computers. Therefore, only CI within one configuration is considered to partly take the electronic correlations into account. Table 1 presents a comparison of the transition energies and oscillator strengths of some transitions of Au^{32+} (ground configuration $4s^24p^64d^{10}4f$), together with the results obtained by several other approaches: 1) relativistic Hartree–Fock (RHF), 2) relativistic many-body perturbation theory (RMBPT), and 3) relativistic perturbation theory with a zero-approximation model potential (RPTMP) from Ref. [33]. It can

Table 1
Transition energies ΔE and absorption oscillator strengths f of transitions of ([Ni]) $4s^24p^64d^{10}nl$–$4s^24p^64d^{10}n'l'$ of Au^{32+}. The closed shells are omitted in the first column. Results obtained by the approaches of relativistic Hartree–Fock (RHF), relativistic many-body perturbation theory (RMBPT), and relativistic perturbation theory with a zero-approximation model potential (RPTMP) are from Ref. [33].

Transitions	ΔE (eV)				f		
	This work	RHF	RMBPT	RPTMP	This work	RHF	RPTMP
$5s_{1/2}$–$5p_{1/2}$	51.67	52.39	51.70	51.50	0.210	0.212	0.195
$5s_{1/2}$–$5p_{3/2}$	93.84	94.42	93.89	91.70	0.778	0.779	0.751
$5p_{1/2}$–$5d_{3/2}$	124.72	124.80	124.95	128.03	1.067	1.067	1.057
$5p_{3/2}$–$5d_{5/2}$	91.14	91.36	91.65	96.03	0.764	0.764	0.379
$5p_{3/2}$–$5d_{3/2}$	82.55				0.076		
$5d_{3/2}$–$5f_{5/2}$	105.55	105.67		103.39	0.901	0.998	0.442
$5d_{5/2}$–$5f_{7/2}$	99.04	99.18		97.69	0.819	0.918	0.267
$5d_{5/2}$–$5f_{5/2}$	96.95				0.040		
$4f_{5/2}$–$5d_{3/2}$	389.86	391.13	389.84	379.41	0.058	0.055	0.042
$4f_{7/2}$–$5d_{5/2}$	392.62	393.99	392.92	381.04	0.058	0.055	0.025
$4f_{5/2}$–$5d_{5/2}$	398.45				0.004		

easily be seen that the transition energies and oscillator strengths predicted by the present work and the RHF method are in excellent agreement. The transition energies predicted by the RMBPT method generally agree with those predicted by the present and RHF methods. However, large discrepancies can be found between the results predicted by the present method and the RPTMP method. For example, the transition energy of $4f_{7/2}$–$5d_{5/2}$ predicted by the RPTMP method is ~10 eV lower than that predicted by the present and RHF methods. The oscillator strengths of $5p_{3/2}$–$5d_{5/2}$, $5d_{3/2}$–$5f_{5/2}$, and $4f_{7/2}$–$5d_{5/2}$ predicted by the RPTMP method are about 50% smaller than those predicted by the present and RHF methods. For the transition of $5d_{5/2}$–$5f_{7/2}$, the oscillator strength predicted by the RPTMP method is smaller than those predicted by the present and RHF methods by a factor of about 3. The RPTMP method uses a zero-approximation model potential and it may be not adequate for such a complex atomic system, where there is a large amount of atomic data for the ion stages with open $4d$ and $4f$ shells. Unfortunately, as far as we know, there are few atomic data in the literature to which comparisons can be made. However, the excellent agreement between the results obtained by the present, RHF and RMBPT results shown in Table 1 indicates that the present atomic data are reliable.

After all atomic data such as energy levels, oscillator strengths and photoionization cross section are obtained in the fine-structure level and relativistic configuration approaches, the radiative opacity can be obtained. As an illustrative example, the radiative opacity of a gold plasma at 100 eV and 0.001 g/cm^3 obtained by using the hybrid model are shown in Fig. 5. At this condition, the dominant ion stages in the gold plasma are Au^{27+}–Au^{32+} accounting for 2.81%, 12.07%, 27.23%, 32.84%, 18.99% and 4.90%, of the population, respectively, which have open $4f$ shells in the ground configurations of $4s^24p^64d^{10}4f^m$ ($m = 6$–1). The radiative opacity obtained by a pure DCA and AA models are shown in panels (a) and (b), respectively. In the calculation by the pure DCA model, the selected configurations are the same as those used in the hybrid model. From the inspection of Fig. 5, one can see that the spectral profile predicted by the DCA model is in generally good agreement with that predicted by the hybrid model. AA model predicts a similar profile as DCA model does in the photon energy range of 0–400 eV and a very gross profile in 400–1300 eV. Both DCA and AA models can not predict the detailed absorption structure as the hybrid model does. For the strongest $4d$–$4f$ transition lines in the photon energy range of 250–300 eV, the hybrid model predicts very complicated absorption structures where the detailed lines merge together. Yet, the DCA and AA models only predict a simple profile for these detailed absorption lines.

In order to show the discrepancies between the three models more clearly, the spectra in the photon energy range of 200–370 eV are redrawn in Fig. 6. It can be seen that both DCA and AA models predict three main absorption features which originate from the transitions of $4p$–$4d$ and $4d$–$4f$ and the line positions predicted by AA model are systematically about 10 eV lower than predicted by DCA model. The positions of $4d$–$4f$ predicted by DCA model is about 20 eV lower than those predicted by the hybrid model. The hybrid model predicts a broad absorption band in the photon energy range of 250–300 eV and the DCA and AA models predict a narrow absorption profile in the lower photon energy range of 250–275 eV. The discrepancies between the spectrally resolved opacity result in discrepancies between associated mean opacities. The Planck mean opacities predicted by the DCA and AA models are 5742 and 5615 cm^2/g, respectively, which are ~15% smaller than that (6444 cm^2/g) predicted by the hybrid model. At the temperature of 100 eV, the Planck weighting function reaches the maximum around photon energy of 290 eV where the spectra predicted by AA and DCA models are in good agreement except that the spectra of AA model are systematically 10 eV lower than those of DCA model. Thus, the Planck mean opacity predicted by DCA and AA models are very close. Yet the hybrid model predicts complicated absorption structures that are much larger than those predicted by DCA and AA models and therefore the Planck mean opacity of the hybrid model is larger than those of DCA and AA models. At the temperature of 100 eV, the Rosseland weighting function reaches the maximum around photon energy of 380 eV where the DCA model predicts detailed absorption structures, as dose the hybrid model and therefore the Rosseland mean opacity predicted by the two models are similar, i.e., they are 679 and 718 cm^2/g, respectively. The agreement of Rosseland mean opacity predicted by the hybrid and DCA models does not mean that the detailed treatment for the transitions is unnecessary. Based on the large discrepancies of spectrally resolved opacity of the hybrid and DCA models in the photon energy range of 280–300 eV, large discrepancies between Rosseland mean opacities should be expected at temperatures of 70–80 eV where the maximum value of the Rosseland weighting function is located. The Rosseland mean predicted by the AA model is 1785 cm^2/g which is nearly 150% larger than that predicted by the hybrid model because AA model

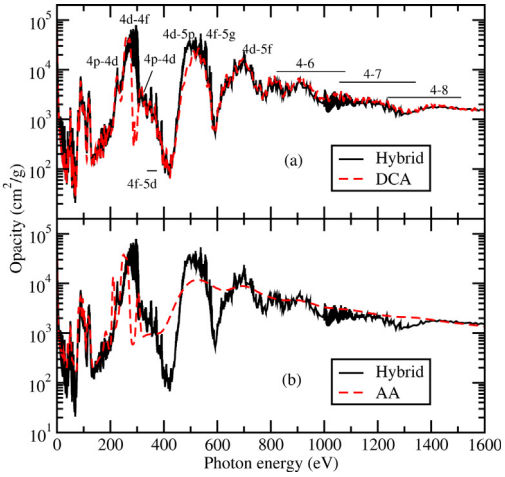

Fig. 5. The spectrally resolved opacities of the gold plasma at 100 eV and 0.001 g/cm^3 in the photon energy range of 0–1600 eV obtained by the hybrid, pure DCA and AA models.

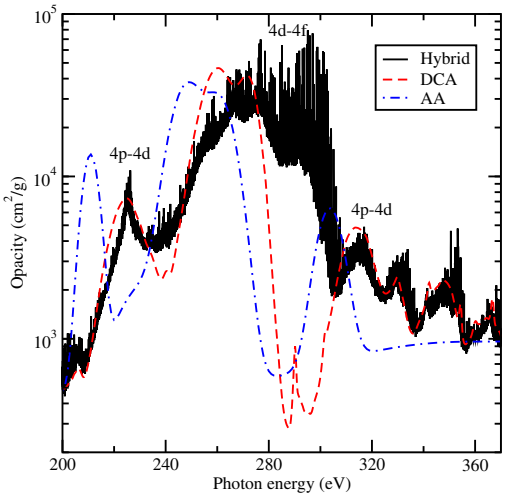

Fig. 6. Same to Fig. 5, but in the photon energy range of 200–370 eV.

does not predict the detailed absorption structures that are predicted by the hybrid model in the photon energy range of 350–400 eV. These large discrepancies indicate that the accurate calculation for the strong transitions is important.

4. Conclusion

In conclusion, a hybrid DLA and DCA method has been developed to calculate the opacities of gold plasmas with open 4*f* and 4*d* shells. To calculate the atomic data as accurately as possible, the DLA method is used for the transitions to lower excited states, saving computational cost, the DCA method is used for the transitions to highly excited states. As an application, the spectrally resolved opacity of gold plasmas at 100 eV and 0.001 g/cm^3 are calculated by using the hybrid model and comparing it with the spectra obtained by pure DCA and AA models. The pure DCA method predicts absorption profiles that are similar to those found using the hybrid method. However, for the DCA and hybrid models the strongest 4*d*–4*f* transitions are not in agreement. That is, the positions of 4*d*–4*f* transitions predicted by the DCA method are about 20 eV lower and the peak line intensities are smaller by a factor of about 2 than the counterparts predicted by the hybrid method. The AA model predicts a similar frequency-dependent structure for the 4*d*–4*f* transitions when compared to the pure DCA method, while the positions are about 10 eV lower. The largest discrepancies mainly originate from the effects of collapse of 4*f* orbitals. Due to the orbital collapse, the electronic correlations are important which are not considered in the DCA and AA model, while the DLA method takes the effects into account by considering the state mixing in each particular configuration. The large discrepancies indicate that the detailed treatment for the collapsed orbitals is necessary. The present hybrid model can be used to investigate the radiative opacities of other high-Z plasmas with complex structures.

Acknowledgment

This work was supported by the National Natural Science Foundation of China under Grants Nos. 11204376, 11274382 and 11274383. Calculations are carried out at the Research Center of Supercomputing Application, NUDT.

References

[1] E. Storm, J. Fusion Energy 7 (1988) 131.
[2] R.L. Kauffman, et al., Phys. Rev. Lett. 73 (1994) 2320.
[3] O.S. Jones, et al., Phys. Rev. Lett. 93 (2004) 065002.
[4] E.L. Dewald, et al., Phys. Rev. Lett. 95 (2005) 215004.
[5] K. Eidmann, A. Bar-Shalom, A. Saemann, G. Winhart, Europhys. Lett. 44 (1998) 459.
[6] Jiyan Zhang, et al., Phys. Plasmas 18 (2011) 113301.
[7] C. Bauche-Arnoult, J. Bauche, M. Klapisch, Adv. Atom. Mol. Phys. 23 (1987) 131.
[8] A. Bar-Shalom, J. Oreg, W.H. Goldstein, D. Shvarts, A. Zigler, Phys. Rev. A 40 (1989) 3183.
[9] J. Yuan, Phys. Rev. E 66 (2002) 047401.
[10] J. Miao, J. Yuan, Phys. Rev. E 69 (2004) 017401.
[11] J. Zeng, J. Yuan, Phys. Rev. E 74 (2006) 025401.
[12] J. Zeng, J. Yuan, Phys. Rev. E 76 (2007) 026401.
[13] J. Zeng, J. Phys. B Atom. Mol. Opt. Phys. 41 (2008) 125702.
[14] J. Yan, Z. Wu, Phys. Rev. E 65 (2002) 066401;
J. Yan, Z. Wu, J. Pang, Y. Qiu, Chin. Phys. Lett. 19 (2002) 818.
[15] Q. Porcherot, J.-C. Pain, F. Gilleron, T. Blenski, High Energy Density Phys. 7 (2011) 234.
[16] R.F. Heeter, S.B. Hansen, K.B. Fournier, et al., Phys. Rev. Lett. 99 (2007) 195001.
[17] R.W. Lee, J.K. Nash, Yu Ralchenko, J. Quant. Spectrosc. Radiat. Transfer 58 (1997) 737.
[18] C. Bowen, A. Decoster, C.J. Fontes, K.B. Fournier, O. Peyrusse, Yu. V. Ralchenko, J. Quant. Spectrosc. Radiat. Transfer 81 (2003) 71.
[19] C. Bowen, R.W. Lee, Yu Ralchenko, J. Quant. Spectrosc. Radiat. Transfer 99 (2006) 102.
[20] J.G. Rubiano, R. Flordo, C. Bowen, R.W. Lee, Yu Ralchenko, High Energy Density Phys. 3 (2007) 225.
[21] C.J. Fontes, J. Abdallah Jr., C. Bowen, R.W. Lee, Y. Ralchenko, High Energy Density Phys. 5 (2009) 15.
[22] C. Gao, F. Jin, J. Zeng, J. Yuan, New J. Phys. 15 (2013) 015022.
[23] A.J. Mackinnon, et al., Phys. Rev. Lett. 108 (2012) 215002.
[24] C. Gao, J. Zeng, Phys. Rev. E 78 (2008) 046407.
[25] R.D. Cowan, Theory of Atomic Spectra, University of California Press, Berkeley, 1981.
[26] J.C. Stewart, K.D. Pyatt Jr., Astrophys. J. 144 (1966) 1203.
[27] M.F. Gu, Astrophys. J. 579 (2002) L103.
[28] U. Becker, et al., Phys. Rev. A 34 (1986) 2858.
[29] J. Migdalek, W. Siegel, Phys. Rev. A 61 (2000) 062502.
[30] M. Habibi, et al., Phys. Rev. A 80 (2009) 033407.
[31] Y. Zou, C.F. Fischer, Phys. Rev. Lett. 88 (2002) 183001.
[32] J. Zeng, G. Zhao, J. Yuan, J. Quant. Spectrosc. Radiat. Transfer 102 (2006) 172.
[33] E.P. Ivanova, Atom. Data Nucl. Data Tables 97 (2011) 1.